Optics Letters

Two-dimensional imaging of electromagnetic fields via light-sheet fluorescence imaging with Rydberg atoms

Noah Schlossberger,[1,*] Tate McDonald,[1,2] Kevin Su,[3] Rajavardhan Talashila,[1,4] Robert Behary,[3] Charles L. Patrick,[1,2] Daniel Hammerland,[1,2] Eugeniy E. Mikhailov,[3] Seth Aubin,[3] Irina Novikova,[3] Christopher L. Holloway,[1] and Nikunjkumar Prajapati[1]

[1]National Institute of Standards and Technology, Boulder, Colorado 80305, USA
[2]Department of Physics, University of Colorado, Boulder, Colorado 80309, USA
[3]Department of Physics, College of William & Mary, Williamsburg, Virginia 23187, USA
[4]Department of Electrical Engineering, University of Colorado, Boulder, Colorado 80309, USA
*noah.schlossberger@nist.gov

Received 1 May 2025; revised 0 Month 2025; accepted 13 October 2025; posted 24 October 2025; published 22 November 2025

Imaging of electric and magnetic fields is limited by the fact that conventional field probes rely on conductive elements that perturb the fields they are meant to measure and require either spatial scanning or arrays to produce field maps. Atomic sensors based on Rydberg states offer a minimally invasive and broadband alternative, enabling absolute field measurements without external calibration. In this work, we present a field imaging technique that combines the spatial resolution of planar laser-induced fluorescence-dip spectroscopy with the field sensitivity and spectral resolution of electromagnetically induced transparency (EIT) using Rydberg states of atomic vapor. By imaging the change in fluorescence due to EIT, we spatially resolve the field-induced shifts in atomic energy levels, enabling the imaging of arbitrary electric field distributions from MHz to tens of GHz at the ~V/cm level and static magnetic fields at the ~mT level. We also image resonant microwave electric fields at the ~5 mV/cm level. This technique achieves a spatial resolution of 160 µm, limited by our camera, with a fundamental resolution limit near 5 µm.

https://doi.org/10.1364/OL.566697

In this manuscript, we demonstrate the capability to image both electric and magnetic fields using a Rydberg atom sensor. Atomic sensors offer unique advantages over conducting antennas and field probes. They do not significantly scatter or absorb fields like conventional probes [1], the same sensor geometry can be used to measure fields from DC to GHz (which would require varying sized antennas [2]), and they do not require calibration to a known field because they relate the field to a measured frequency with atomic properties and SI constants [3]. The earliest techniques for atomic electric field sensors used laser-induced fluorescence [4]. This was extended to two-dimensional imaging by forming the laser beam into a light-sheet and imaging the resulting sheet of fluorescence [5]. The spectral resolution was then enhanced with two-photon fluorescence-dip spectroscopy [6]. Planar laser-induced fluorescence-dip (LIF-dip) spectroscopy has been used to image electric fields on the order of hundreds of V/cm, limited by the low polarizabilities of the relevant states [7–10] or the spectral resolution of the detection scheme [11].

Rydberg atoms make much more sensitive electric field probes due to their large polarizabilities and electric dipole moments [12]. These states can be probed with spectral linewidths on the order of MHz using two-photon electromagnetically induced transparency (EIT) [13], allowing field sensitivities as low as 5nV/(cm$\sqrt{\text{Hz}}$) [14]. However, the application of this sensing scheme to imaging has been limited. Raster scanning this readout scheme [15–17] integrates along the vapor cell, useful only for measuring field distributions that are uniform in one dimension. Crossing the laser beams to localize the measurement significantly reduces the spectral linewidth [18]. Imaging of a narrow band of THz radiation resonant with a Rydberg-Rydberg transition has been performed via induced population transfer from the THz field [19,20], but this only works for a discrete set of frequencies of THz radiation. We present a technique that merges the spatially resolved sensing scheme of planar LIF-dip spectroscopy with the sensitivity of electromagnetically induced transparency readout of Rydberg states of alkali atoms. This allows for imaging of arbitrary (off-resonant) electric fields at the single V/cm level, orders of magnitude more sensitive than previous LIF-dip measurements, and resonant RF fields at the mV/cm level. This technique is quite general as it can measure a variety of fields based on their perturbation of the atomic spectrum: we also demonstrate the ability to measure magnetic fields at the mT level without modification to the setup.

The measurement scheme is shown in Fig. 1. Ground state atoms are coupled to a Rydberg state via a two-photon lad-

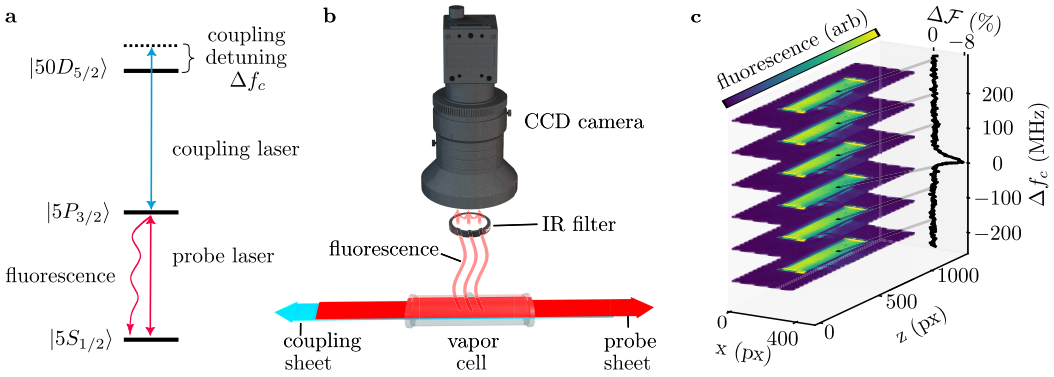

Fig. 1. The fluorescence measurement scheme. (a) The energy level diagram for ^{85}Rb. (b) The experimental setup. (c) The CCD image of the light-sheet is recorded as the coupling laser is scanned (Δf_c). The change in fluorescence $\Delta\mathcal{F}$ of at a single point is shown.

der EIT scheme (Fig. 1(a)) with a 780 nm probe (630 µW) and 480 nm coupling (380 mW) laser. With the probe locked on resonance using a reference vapor cell, the detuning of the coupling laser (Δf_c, referenced to EIT in the reference cell) is scanned and the fluorescence decreases when the coupling laser is on resonance, thus reading out the energy of the Rydberg state. The probe and coupling beams are formed into 12 mm flat top by 1 mm Gaussian full-width at half-maximum light-sheets using anamorphic prism pairs and cylindrical lenses (Fig. 1(b)), and are sent into the room temperature vapor cell counter-propagating to partially cancel the Doppler shift. The fluorescence passes through a 780 ± 5 nm optical bandpass filter and is imaged by a charge-coupled device (CCD) camera with a compound lens focused on the plane of the beams. The coupling laser's detuning Δf_c is scanned as the camera records the fluorescence, so the time axis gives a spectrum at each point on the image (Fig. 1(c)). The fluorescence spectrum is measured to have a Gaussian one-sigma width of 9.9± 0.2 MHz.

Non-resonant electric fields can be measured via their induced Stark shift on the Rydberg state. Generally, each angular momentum substate m_J will undergo a different shift, causing the spectrum to split into different peaks. The frequency shift on each m_J level due to the Stark shift for weak electric fields is given by:

$$\Delta f_{\text{Stark}}(m_J, E) \approx -\frac{1}{2}\alpha_{m_J} E^2/h, \tag{1}$$

where α_{m_J} is the polarizability of the state, h is Planck's constant, and E is the root-mean-square (RMS) value of the electric field. To detect electric fields via their Stark shift, they must shift the states by more than one linewidth, typically requiring fields on the order of V/cm. In this regime, the response is no longer quadratic, as avoided crossings begin to repel nearby states. To account for this, we numerically calculate a Stark Map using the ARC python package [21] to find the Stark shifts $\Delta f_{\text{Stark}}(m_J, E)$. We can then fit our spectrum to a sum of Gaussians at the measured EIT linewidth σ with an empirical set of weights A_{m_J} in order to extract the field:

$$\Delta\mathcal{F}_{\text{Stark fit}} = \sum_{m_J} A_{m_J} \exp\left(-\frac{(\Delta f_c - \Delta f_{\text{Stark}}(m_J, E))^2}{2\sigma^2}\right), \tag{2}$$

To demonstrate the electric field imaging capability, we apply a 30 MHz tone to a microstrip line (Fig. 2(a)). We place a matte black paper over the transmission line to prevent reflections, place an 11× 11× 45 mm vapor cell above it, and image using the technique described above. This demonstrates the field imaging capability in the quasi-electrostatic regime where the spatial variations are small compared to the wavelength. To demonstrate imaging in the regime where the spatial variations are of order a wavelength, we image the field in a two wire transmission line with an open end (Fig. 2(b)). The wires are separated by 11 mm and are 75 mm long, and a 10 mm diameter × 75 mm length cylindrical vapor cell is placed inside. The reflection at the open end creates well-defined standing modes which vary along z. We apply 15 dBm of power and measure the fields at 1 GHz where one half-wavelength fits along the transmission line, at 5 GHz where about three full wavelengths fit along the transmission line, and at 10 GHz where about six full wavelengths fit along the transmission line.

If a microwave field is at a frequency resonant with a Rydberg-Rydberg transition, the Rydberg states of the atom are much more sensitive to it, and therefore, much weaker fields can be detected. Resonant radiation leads to Autler-Townes splitting of the Rydberg state, in which the EIT peak splits into two peaks separated by a frequency Δf_{AT} of [13]:

$$\Delta f_{\text{AT}} = \frac{\mu_{\text{RF}} E}{h}, \tag{3}$$

where E is the peak value of the applied resonant electric field, and μ_{RF} is the transition dipole moment of the Rydberg-Rydberg transition. We can thus determine the field by fitting the EIT spectrum to:

$$\Delta\mathcal{F}_{\text{AT fit}} = \exp\left(\frac{-\left(\Delta f_c - \frac{\mu_{\text{RF}}E}{2h}\right)^2}{2\sigma^2}\right) + \exp\left(\frac{-\left(\Delta f_c + \frac{\mu_{\text{RF}}E}{2h}\right)^2}{2\sigma^2}\right). \tag{4}$$

Dipole moments for these transitions tend to be on the order of 2 GHz/(V/cm), allowing fields on the order of 5 mV/cm to be detected. The drawback of this sensing mode is two-fold. First, only a discrete set of frequencies can be detected, and changing between them requires tuning the coupling laser on the order of nm (although there are methods to continuously tune the Rydberg resonance [22–24]). Second, these transitions tend to be between 5 and 40 GHz. In this regime, the wavelength is not large compared to the geometry of the vapor cell, meaning that the vapor cell walls are partially reflected, and standing waves will form between them [15,25]. These standing waves are imaged in an 11× 11× 45 mm cell at 17.041 GHz, resonant with the

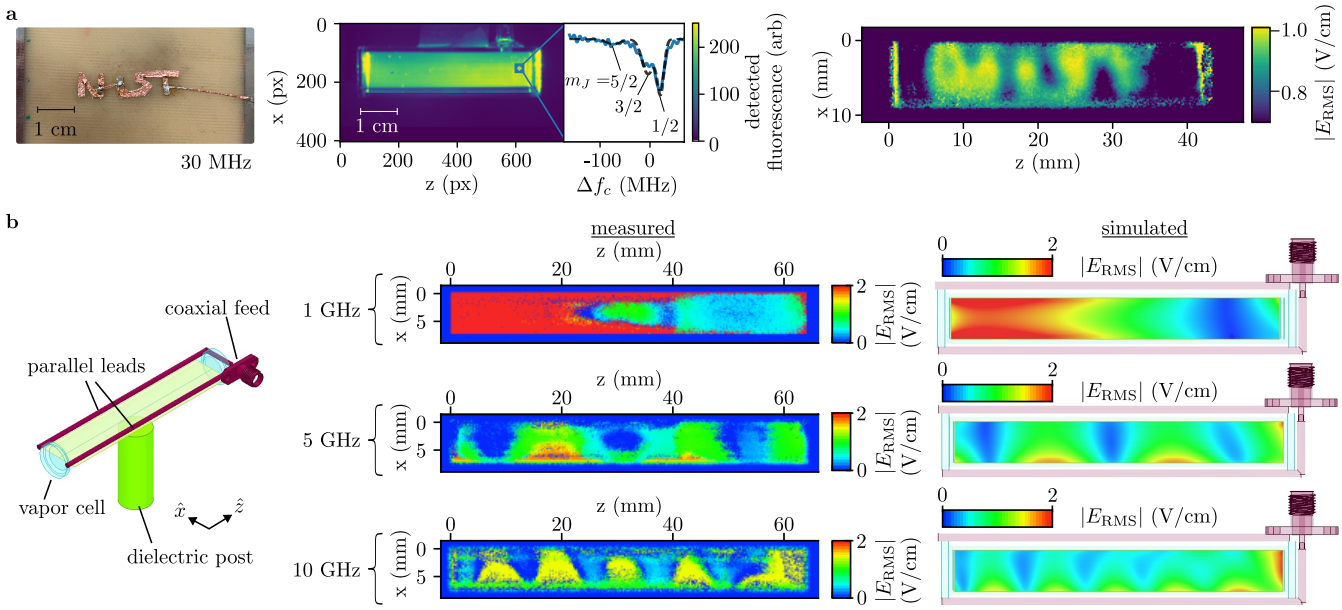

Fig. 2. Fluorescence E-field images utilizing the AC Stark shift. (a) A conducting strip is placed over a sheet of insulator with the bottom grounded, and a 30 MHz voltage is applied to the strip. A vapor cell is placed above it and the fluorescence is imaged and fit (middle) to produce a mapping of the electric field (right). (b) An open-ended twin lead transmission line generates standing waves in the vapor cell. The simulated (middle) and measured (right) field distributions for various frequencies are shown.

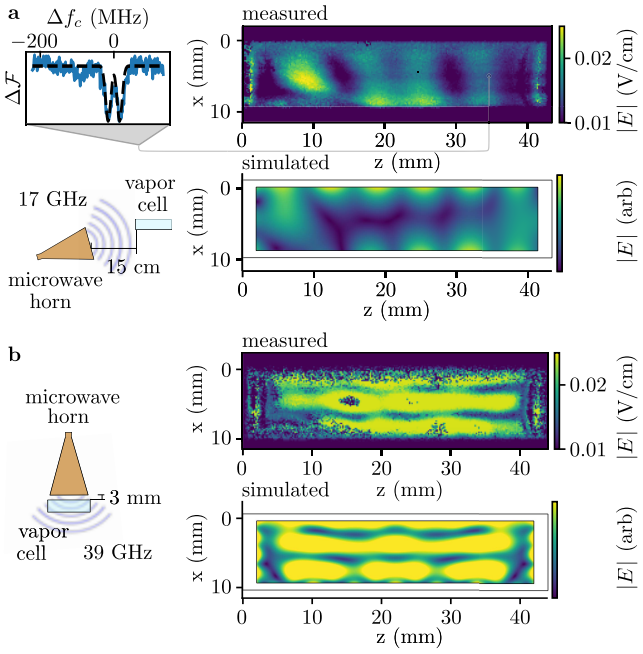

Fig. 3. Fluorescence E-field images utilizing resonant Autler-Townes splitting. (a) Measured (top) and simulated (bottom) field distributions of standing waves from a 17.041 GHz tone applied from the bottom left. (b) Field distribution of standing waves from a 39.385 GHz tone applied from the top. The simulations assume an incident plane wave as modeling the horn geometry is computationally intractable.

$50D_{5/2} \rightarrow 51P_{3/2}$ transition, and at 39.385 GHz, resonant with the $50D_{5/2} \rightarrow 52P_{3/2}$ transition in Fig. 3.

Strong magnetic fields can also be measured with fluorescence light-sheet imaging of EIT by their induced Zeeman shift on the Rydberg states. While this method is not as sensitive as other atomic magnetometry techniques [26,27], it can be used with the same setup described above to measure fields on the order of mT. The shape of EIT spectra for Rydberg states in the presence of magnetic fields is described in Ref. [28]. The spectrum is predominantly composed of $m_J = \pm 5/2$, which shifts in the spectrum in opposite directions at a rate of $\mu_{\mathrm{eff}} = 20.4$ MHz/mT. By measuring the shift of the $m_J = \pm 5/2$ levels, we can then deduce the magnitude of the field. Vector information can be gained by considering the distribution of m_J levels. Magnetic fields at the mT level are strong enough to set the preferred quantization axis [28], meaning the optical light will appear to have different polarizations depending on this projection. To make use of this, we use circularly polarized σ^- light in the z axis, such that if the magnetic field is in the $+z$ direction it will preferentially populate the $m_J = -5/2$ state, and the magnetic field is in the $-z$ direction it will preferentially populate the $m_J = +5/2$ state. When the magnetic field is perpendicular to the probe, the $+5/2$ and $-5/2$ states will be equally populated. Thus, from the ratio of these two states on the spectrum, we can get the projection of the field onto the z-axis independently from the magnitude of the field. These two thus give the magnitude and sign of the z component of the field, and the magnitude of the orthogonal component of the field (in 2D, this is the x-component). The sign of the x-component cannot be determined from this measurement. To demonstrate magnetic field imaging, we placed two permanent bar magnets 85 mm apart with their magnetic north poles facing each other in the x-axis such that they generate a quadrupole field. We then performed fluorescence imaging with an 11× 11× 45 mm rectangular vapor cell in the center of the quadrupole. The results are shown in Fig. 4. At each point, we fit the normalized fluorescence spectrum to a sum of two Gaussians representing the two dominant m_J states:

$$\Delta \mathcal{F}_{B\,\mathrm{fit}} = \cos^2\left(\frac{\theta}{2}\right) \exp\left(\frac{(\Delta f_c + \mu_{\mathrm{eff}} B)^2}{2\sigma^2}\right)$$

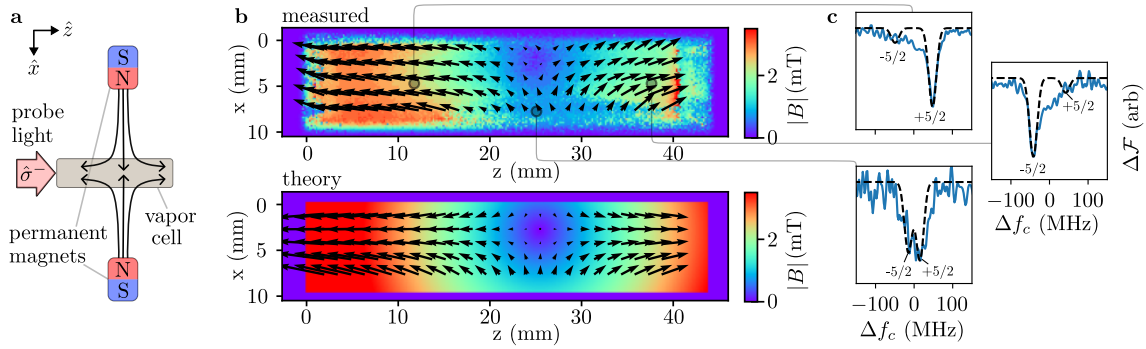

Fig. 4. Fluorescence B-field image utilizing Zeeman splitting. (a) Diagram of the setup. (b) Measured (top) and theoretical (bottom, Eq. (6)) magnetic field magnitude and vector. Because the direction of the x-component (vertical component) of the magnetic field is ambiguous, they are plotted pointing upwards. (c) Spectra and fits of the fluorescence at three different field directions.

$$+\sin^2\left(\frac{\theta}{2}\right)\exp\left(\frac{(\Delta f_c-\mu_{\text{eff}}B)^2}{2\sigma^2}\right), \qquad (5)$$

where B is the applied magnetic field and θ is the angle of the magnetic field from the z-axis. The results are consistent with an ideal magnetic quadrupole, which takes the form:

$$B_{\text{quadrupole}}=\frac{3\mu_{\text{magnet}}\mu_0}{\pi\, r_{\text{magnet}}^4}\left((z-z_0)\hat{z}-(x-x_0)\hat{x}\right), \qquad (6)$$

where (x_0, z_0) is the center of the quadrupole, r_{magnet} is the distance from this point to one of the magnets, μ_0 is the permeability of free space, and μ_{magnet} is the magnetic dipole moment of each magnet, measured using a calibrated magnetometer to be 0.494±0.001 A·m^2 (see Supplement 1).

Spatial resolution of this imaging technique is fundamentally limited by thermal motion of the atoms causing a distance between the absorption and re-emission of the probe photons, providing a blurring of the spectral image of 5 µm at room temperature. In practice, our resolution was limited to 160 µm by the projected pixel size of our imaging system, and the spatial averaging we performed to achieve a good signal-to-noise ratio (SNR). The minimum detectable field is set by the requirement that the fields need to shift or split the spectrum by order of one linewidth to be resolved, limiting AC stark detection to the order of V/cm, Autler-Townes to the order of 5 mV/cm, and Zeeman shifts to the order of mT. The time resolution is severely limited by the integration time required to achieve SNR. We scanned the coupling laser over 250 MHz with a scan period of 10 s and record images at a framerate of 100 Hz, resulting in a spectral resolution of 250 kHz. We average the increasing- and decreasing-frequency scans, resulting in a total measurement time of 20 s per image. The time and optical resolution could be improved by using a larger focusing lens and moving the camera closer, allowing less spatial and temporal averaging to reach SNR.

Funding. National Science Foundation (2326736); U.S. Department of Energy (DE-AC05-06OR23177); National Institute of Standards and Technology

Disclosures. The authors declare no conflicts of interest.

Data availability. The data related to the findings of this paper are publicly available at [29].

Supplemental document. See Supplement 1 for supporting content.

REFERENCES

1. M. Noaman, H. Amarloo, R. Pandiyan, *et al.*, in *Quantum Sensing, Imaging, and Precision Metrology*, J. Scheuer and S. M. Shahriar, eds., International Society for Optics and Photonics (SPIE, 2023), Vol. **12447**, p. 124470V.
2. D. M. Pozar, *Microwave Engineering*, 3rd ed. (Wiley, 2005).
3. C. L. Holloway, J. A. Gordon, S. Jefferts, *et al.*, IEEE Trans. Antennas Propag. **62**, 6169 (2014).
4. K. Takiyama, K. Kadota, T. Oda, *et al.*, Rev. Sci. Instrum. **59**, 2351 (1988).
5. R. K. Hanson, J. Quant. Spectrosc. Radiat. Transf. **40**, 343 (1988).
6. U. Czarnetzki, D. Luggenhölscher, and H. F. Döbele, Phys. Rev. Lett. **81**, 4592 (1998).
7. U. Czarnetzki, D. Luggenhölscher, and H. F. Döbele, Plasma Sources Sci. Technol. **8**, 230 (1999).
8. E. V. Barnat and G. A. Hebner, J. Appl. Phys. **96**, 4762 (2004).
9. T. Kampschulte, J. Schulze, D. Luggenhölscher, *et al.*, New J. Phys. **9**, 18 (2007).
10. E. V. Barnat and G. A. Hebner, J. Appl. Phys. **97**, 063301 (2005).
11. W. An, Z. Wang, A. Weisenburger, *et al.*, Rev. Sci. Instrum. **93**, 023503 (2022).
12. N. Schlossberger, N. Prajapati, S. Berweger, *et al.*, Nat. Rev. Phys. **6**, 606 (2024).
13. J. A. Sedlacek, A. Schwettmann, H. Kübler, *et al.*, Nat. Phys. **8**, 819 (2012).
14. M. Cai, S. You, S. Zhang, *et al.*, Appl. Phys. Lett. **122**, 161103 (2023).
15. C. L. Holloway, J. A. Gordon, A. Schwarzkopf, *et al.*, Appl. Phys. Lett. **104**, 244102 (2014).
16. H. Q. Fan, S. Kumar, R. Daschner, *et al.*, Opt. Lett. **39**, 3030 (2014).
17. L. Ma, E. Paradis, and G. Raithel, Opt. Express **28**, 3676 (2020).
18. K. Su, R. Behary, S. Aubin, *et al.*, J. Opt. Soc. Am. B **42**, 757 (2025).
19. C. G. Wade, N. Šibalić, N. R. de Melo, *et al.*, Nat. Photonics **11**, 40 (2017).
20. L. A. Downes, A. R. MacKellar, D. J. Whiting, *et al.*, Phys. Rev. X **10**, 011027 (2020).
21. E. Robertson, N. Šibalić, R. Potvliege, *et al.*, Comput. Phys. Commun. **261**, 107814 (2021).
22. S. Berweger, N. Prajapati, A. B. Artusio-Glimpse, *et al.*, Phys. Rev. Appl. **19**, 044049 (2023).
23. J. Hu, H. Li, R. Song, *et al.*, Appl. Phys. Lett. **121**, 014002 (2022).
24. M. T. Simons, A. B. Artusio-Glimpse, C. L. Holloway, *et al.*, Phys. Rev. A **104**, 032824 (2021).
25. H. Fan, S. Kumar, J. Sheng, *et al.*, Phys. Rev. Appl. **4**, 044015 (2015).
26. J. Li, W. Quan, B. Zhou, *et al.*, IEEE Sensors J. **18**, 8198 (2018).
27. J. Kitching, S. Knappe, V. Shah, *et al.*, in Frequency Control Symposium, 2008 IEEE International (2008), p. 789.
28. N. Schlossberger, A. P. Rotunno, A. B. Artusio-Glimpse, *et al.*, Phys. Rev. A **109**, L021702 (2024).
29. N. Schlossberger, T. McDonald, and K. Su,"Public Data resource data associated with 'Two-dimensional imaging of electromagnetic fields via light sheet fluorescence imaging with Rydberg atoms'," NIST (2025), https://doi.org/10.18434/mds2-3650.